Journal of Materials Chemistry C

ROYAL SOCIETY OF CHEMISTRY

PAPER

View Article Online
View Journal | View Issue



Cite this: J. Mater. Chem. C, 2024, 12, 8944

# Self-powered solar-blind ultraviolet-visible $Cu_2O/Ga_2O_3$ photodetectors†

Xiaodan Wang,[ab] Jianping Xu,* [a] Shaobo Shi,[c] Lina Kong,[b] Xiangwei He,[a] Jiahang He,[a] Xiaosong Zhang [b] and Lan Li*[b]

Traditional optical communication using single narrow-band photodetectors (PDs) has poor confidentiality because all information and data are exposed to free space. With the development of science and technology, even the optical communication in the solar-blind ultraviolet (UV) band carries the risk of eavesdropping. Dual-band PDs have potential applications in secure and reliable optical communication through a combination of optical encryption and algorithmic encryption. In this paper, self-powered $Cu_2O/Ga_2O_3$ heterojunction PDs with solar-blind UV-visible photodetection were fabricated. By adjusting the pH value of the $Cu_2O$ electrolyte, the crystallization quality and grain orientation of the $Cu_2O$ thin film were improved, and the interface transfer resistance of the heterojunctions was decreased. The $Cu_2O/Ga_2O_3$ PDs fabricated in $Cu_2O$ electrolyte with a pH value of 9.5 demonstrated the optimized solar-blind UV-visible photoresponse characteristics. In the absence of applied bias, the device exhibited a responsivity of 0.12 mA $W^{-1}$, a rise time of 2.48 ms and a fall time of 11.72 ms at 254 nm. The responsivity reaches 19 mA $W^{-1}$ when illuminated at 475 nm, and the rise and fall times are 0.96 and 9.12 ms, respectively. Utilizing the excellent photoresponse characteristics of the solar-blind UV-visible band, the device was used to design and demonstrate a proof-of-concept optical communication system for secure data transmission. The proposed system features two independent light channels, utilizing solar-blind UV light as the information carrier and visible light for key transmission. By implementing specific algorithms, this design ensures safe and reliable communication.

Received 11th March 2024,
Accepted 22nd May 2024

DOI: 10.1039/d4tc00965g

rsc.li/materials-c



## 1. Introduction

Single narrow-band photodetectors (PDs) cannot meet the requirements of high-precision target detection and information recognition. The dual-band and multi-band PDs can utilize the difference of photoresponse characteristics in the bands to realize mutual verification and mutual compensation of information, and then improve the accuracy, precision and safety of data. Among the dual-band PDs including visible-near-infrared,[1–3] UV-near-infrared,[4,5] blue-red,[6] near-infrared-short infrared,[7] and UV-visible,[8–10] UV-visible dual-band PDs are widely used in flame detection, memory storage and secure communication.[11–16] Compared with the combination of multi-band PDs and line-array multi-band PDs, the PDs that achieve dual-band or even multi-band detection through a single device have the advantages of simple structure and reduced interference. The earliest multi-band single PDs were fabricated using quantum well materials utilizing the sub-band transition formed in the conduction band of doped quantum wells. Devices such as two-color PDs with a GaAlAs/GaAs quantum well structure have advantages such as flexible wavelength control and a simple preparation method.[17] The emerging heterojunction PDs constructed using semiconductors with light absorption in different wavelength bands can realize dual-band or multi-band detection. For example, Wang *et al.* fabricated PDs based on $MoS_2$/Si heterojunctions demonstrating a photoresponse band from the visible to infrared region.[18] He *et al.* constructed the UV-infrared PDs based on β-$Ga_2O_3$/BP heterojunctions.[5]

The direct ultra-wide bandgap $Ga_2O_3$ semiconductor material has a large optical absorption coefficient in the solar-blind UV band, good thermal stability and high breakdown voltage resistance, making it one of the preferred materials for solar-blind UV detectors.[19–21] A $Ga_2O_3$ thin film is generally polycrystalline. Many grain boundaries in $Ga_2O_3$ have a strong

[a] Tianjin Key Laboratory of Quantum Optics and Intelligent Photonics, School of Science, Tianjin University of Technology, Tianjin 300384, China. E-mail: xjp0335@163.com
[b] School of Materials Science and Engineering, Key Laboratory of Display Materials and Photoelectric Devices, Ministry of Education, and Tianjin Key Laboratory for Photoelectric Materials and Devices, Tianjin University of Technology, Tianjin 300384, China. E-mail: lilan2000us@126.com
[c] School of Science, Tianjin University of Technology and Education, Tianjin 300222, China

† Electronic supplementary information (ESI) available. See DOI: https://doi.org/10.1039/d4tc00965g

scattering and blocking effect on carrier transport, resulting in the decrease of photocurrent and responsivity of $Ga_2O_3$ PDs. Some strategies have been proposed to solve this problem from the perspectives of the crystalline quality and the control of crystal plane orientation of $Ga_2O_3$. Some studies have reported an improvement in the device performance by preparing ordered $Ga_2O_3$ nanostructures. The ordered nanorod arrays (NRs) can serve as trapping structures to enhance the light absorption, form interfaces for the separation of photogenerated charge carriers, and provide directional paths to promote carrier transmission.[22–25] In order to achieve the photoresponse characteristics in the solar-blind UV-visible band for $Ga_2O_3$ based PDs, $Ga_2O_3$ is usually compounded with a semiconductor with strong visible light absorption to construct heterojunction PDs, such as $Ga_2O_3$/Au/$MAPbBr_3$ sandwich structure PDs[26] and $Ga_2O_3$/CuSCN core–shell structure PDs.[11] Due to a strong absorption in the visible region, simple preparation and easy control of the crystal phase, $Cu_2O$ is suitable to construct the visible light PDs. The composite of $Cu_2O$ and $Ga_2O_3$ can produce heterojunction PDs with photoresponse characteristics in the solar-blind UV-visible band.

The light absorption coefficient and carriers transport capability of $Cu_2O$ films are closely related to crystallization and grain orientation, which are key factors that determine the photoelectric characteristics of the device.[27] The electrochemical deposition conditions such as the electrolyte substances, concentration and pH value, deposition temperature, time, and current density or voltage can affect the morphology and crystallization of $Cu_2O$ films. Herein, $Cu_2O$ thin films were electrochemical deposited on $Ga_2O_3$ NRs. The morphology and crystal plane orientation of $Cu_2O$ crystals was regulated by controlling the pH value of the electrolyte. The self-powered photoresponse characteristics of $Cu_2O/Ga_2O_3$ heterojunction PDs in the solar-blind UV-visible band were investigated. The self-powered photoresponse characteristics have been elaborated based on the interface contact and optoelectronic properties of $Cu_2O/Ga_2O_3$ heterojunctions. The PDs have been designed and demonstrated a proof-of-concept optical encryption communication system for secure data transmission utilizing the solar-blind UV light as an information carrier and visible light for key transmission.

## 2. Results and discussion

### 2.1 Morphology, crystal structure and optical properties of $Cu_2O/Ga_2O_3$ heterojunctions

Fig. 1 shows SEM images of $Ga_2O_3$ and $Cu_2O$ films deposited on $Ga_2O_3$ with electrolyte solution of different pH values. As can be seen from Fig. 1(a), $Ga_2O_3$ nanorods grow vertically on the FTO substrate with diamond-shaped end faces, a long diagonal length of 100–200 nm and an average length of about 660 nm. The diamond shaped end face is not detected after $Cu_2O$ deposition, and pyramid shaped $Cu_2O$ particles form a continuous and dense film.[28] EDS results of top view and profile view in Fig. S1 (ESI†) suggested that the elements Ga, O and Cu are uniformly distributed throughout the film, indicating that $Cu_2O$ grows on the top and side walls of $Ga_2O_3$ nanorods. With the increase of electrolyte pH of $Cu_2O$, the pyramid-shaped particles of $Cu_2O$ thin films are transformed from tetrahedron to trihedron. $Cu_2O(9)$ and $Cu_2O(9.5)$ thin films are quadrangular pyramids, and the distribution of the particle size becomes more uniform with the increased pH value, whereas the particles of $Cu_2O(10)$ film demonstrate tetrahedral and trihedral pyramid shapes. The pH value of the deposition solution can affect the growth rate of $Cu_2O$ crystals on different crystalline surfaces, and then affects the orientation of the crystal structure of the film and the particle shapes. The oxygen atom density of the $Cu_2O$ (111) crystalline surface is greater than that of the (200) crystalline surface. The electrolytes with smaller pH provide fewer oxygen atoms, which facilitates the rapid growth of the (200) crystalline surface with tetrahedral pyramid shapes. With the increase of the electrolyte pH value, the growth rate of the (111) crystalline surface with higher oxygen atom density gradually exceeds that of the (200) crystalline surface.[29] Therefore, particles of the $Cu_2O(10)$ film show trihedral pyramid shapes and tetrahedral pyramid shapes. The SEM profiles demonstrate that the thickness of the $Cu_2O/Ga_2O_3$ film increases with the increase of the electrolytic pH of $Cu_2O$. The thickness of the $Ga_2O_3$ nanorod film is about 660 nm, and that of the $Cu_2O/Ga_2O_3$ film is 680, 730 and 810 nm for $Cu_2O(9)/Ga_2O_3$, $Cu_2O(9.5)/Ga_2O_3$ and $Cu_2O(10.5)/Ga_2O_3$, respectively. Increase of electrolytic pH of $Cu_2O$ is favorable to accelerate the deposition of $Cu_2O$ particles.

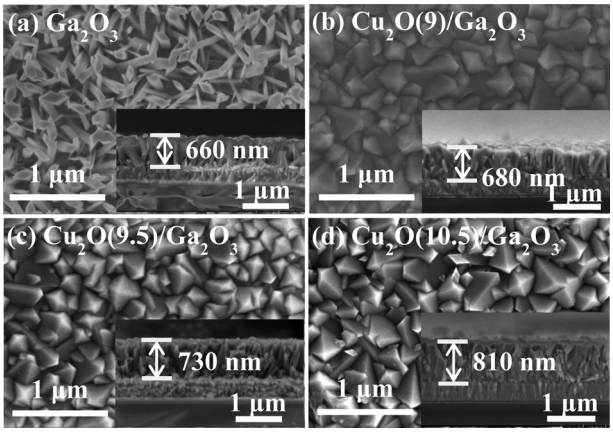


Fig. 1 The top-view and cross-sectional view of SEM images of (a) $Ga_2O_3$ NRs and (b) $Cu_2O(9)/Ga_2O_3$, (c) $Cu_2O(9.5)/Ga_2O_3$ and (d) $Cu_2O(10.5)/Ga_2O_3$.

Fig. 2(a) shows XRD spectra of $Ga_2O_3$ and $Cu_2O$ films deposited on $Ga_2O_3$ with different pH electrolyte solutions. In the XRD patterns of $Ga_2O_3$, the stronger diffraction peak at 36° is attributed to the α-$Ga_2O_3$ (110) crystal plane of corundum-type structure. No peaks of the other phase were found except for the diffraction peaks originated from the FTO substrate.[30] After the electrochemical deposition of $Cu_2O$ thin films on $Ga_2O_3$ substrate, $Ga_2O_3$ retains a corundum-type structure and presents a (110) crystal plane diffraction peak. The (110), (111), (200) and (311) crystal plane diffraction peaks

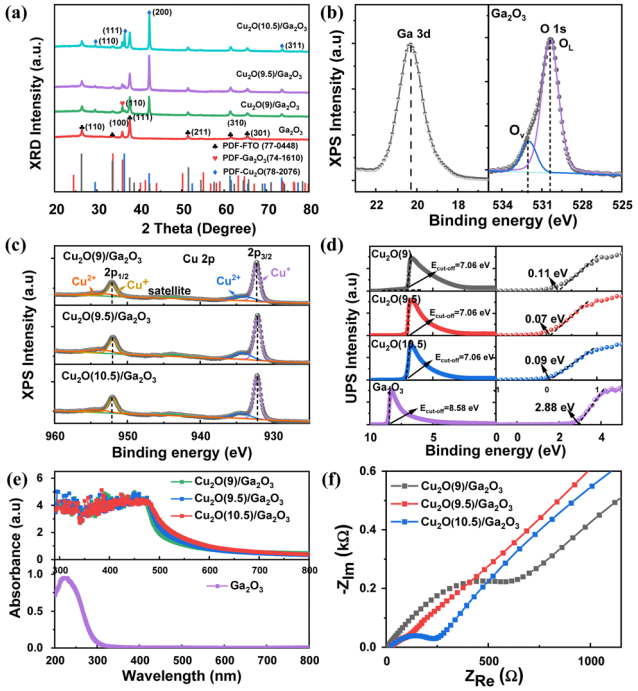


Fig. 2 (a) XRD patterns for $Cu_2O/Ga_2O_3$ with $Cu_2O$ prepared at different pH values. (b) XPS spectra of O 1s and Ga 3d for $Ga_2O_3$. (c) XPS spectra of Cu 2p for $Cu_2O$ prepared at different pH values. (d) VB spectra and UPS spectra for $Ga_2O_3$ and $Cu_2O$ prepared at different pH values. (e) UV-vis absorption spectra for $Ga_2O_3$ and $Cu_2O/Ga_2O_3$ with $Cu_2O$ prepared at different pH values. (f) EIS curves for $Cu_2O/Ga_2O_3$ with $Cu_2O$ prepared at different pH values.

of $Cu_2O$ were observed at 29.6°, 36.5°, 42.4° and 73.6°, while no other phases of Cu and $Cu_xO$ were found.[31,32] With the increase of $Cu_2O$ electrolyte pH, the crystal diffraction intensity of the main diffraction peak (200) of $Cu_2O$ increases, and the (111) crystal diffraction peak of $Cu_2O(10)$ is significantly enhanced compared to the other films, which correlates with the trihedral pyramidal shapes of $Cu_2O$ particles.

The valence states of the elements in $Ga_2O_3$ and $Cu_2O/Ga_2O_3$ were analysed using XPS spectroscopy. Fig. 2(b) shows the XPS spectra of Ga 3d and O 1s of $Ga_2O_3$, and the Ga 3d peak corresponds to a binding energy of 20 eV, which is consistent with the results reported in the literature.[33] The peak shape of O1s is asymmetric and can be fitted to two peaks at 530.4 ($O_L$) and 531.9 eV ($O_V$), where $O_L$ is related to oxygen ions in the lattice and $O_V$ is related to oxygen vacancies.[34,35] Fig. 2(c) shows the XPS spectra of Cu 2p for $Cu_2O$ films deposited on $Ga_2O_3$ substrates with different pH electrolytes. Upon fitting, the peaks related to Cu $2p_{3/2}$ and Cu $2p_{1/2}$ of $Cu^+$ appeared at the binding energies of 932.4 and 952.3 eV, and peaks related to $Cu^{2+}$ appeared at 934.5 and 954.7 eV, which is due to the oxidation of $Cu_2O$ films in air.[36] Combined with the Auger spectrum of Cu in Fig. S2 (ESI†), Cu mainly exists in the form of $Cu^+$ in $Cu_2O$ films.

The band structure of $Ga_2O_3$ and $Cu_2O$ electrons was analyzed by using UPS valence band (VB) spectra of Fig. 2(d). Through the linear extrapolation of the cut-off edge of the Au standard sample in the low energy region, it is calculated that the Fermi level ($E_F$) is −7.96 eV under the bias of −10 V. The $E_F$ values of $Ga_2O_3$ and $Cu_2O$ are calculated using the semiconductor work function formula $\Phi = (E_{cut\text{-}off} - E_F) - 21.22$, in which the cutoff energy ($E_{cut\text{-}off}$) can be linearly extrapolated from the cutoff edge of the high energy region. The $E_{cut\text{-}off}$ for $Ga_2O_3$ and $Cu_2O$ are −8.58 and −7.06 eV, respectively. The calculated $E_F$ are −4.69 and −6.2 eV for $Ga_2O_3$ and $Cu_2O$, respectively. The energy difference between the $E_F$ and the valence band maximum (VBM) of $Ga_2O_3$ and $Cu_2O$ can be analyzed by the intersection of the tangent line at the maximum of the slope and the line along the outer edge of the baseline, which are 2.88, 0.11, 0.07 and 0.09 eV for $Ga_2O_3$, $Cu_2O(9)$, $Cu_2O(9.5)$ and $Cu_2O(10)$, respectively. Combining the optical band gap energies of $Ga_2O_3$ (4.61 eV) and $Cu_2O$ (2.07 eV) calculated from diffuse reflectance spectroscopy (Fig. S4, ESI†), the position of $E_F$ relative to vacuum energy levels can be obtained. The $E_F$ position of $Ga_2O_3$ is far from the VBM, indicating that $Ga_2O_3$ is an n-type semiconductor, whereas the $E_F$ position of $Cu_2O$ is close to the VBM, suggesting that $Cu_2O$ is a p-type semiconductor. The UV-vis absorption spectra of Fig. 2(e) shows that $Ga_2O_3$ has a strong optical absorption in the deep UV region less than 250 nm, and the absorption edge is broadened to about 298 nm, which is related to the deep-level oxygen vacancy defect in $Ga_2O_3$.[37,38] $Cu_2O/Ga_2O_3$ has strong optical absorption from the solar-blind UV to the blue light region, indicating that the composite material can be used for solar-blind UV-visible light detection.

Electrochemical impedance spectroscopy (EIS) can reflect the characteristics of charge transfer at the interface of semiconductor materials. The EIS curves of $Cu_2O/Ga_2O_3$ tested at open-circuit voltage and frequency in the range of 0.1–$10^6$ Hz are given in Fig. 2(f). The radius of the semicircle in the Nyquist plot is related to the interfacial charge transfer process.[39] The size of the radius of the semicircle located in the low-frequency region is related to the charge transfer between $Cu_2O$ and the electrolyte, and the radius of the semicircle located in the high-frequency region is related to the charge transfer at the $Cu_2O/Ga_2O_3$ heterojunction interface. With the increase of $Cu_2O$ electrolyte pH, the radius of the $Cu_2O/Ga_2O_3$ heterojunction semicircle firstly decreases and then increases, indicating the interfacial transfer resistance of $Cu_2O(9.5)/Ga_2O_3$ is the smallest, which is favorable for the transfer of photogenerated carriers.

### 2.2 Self-powered photoresponse characteristics of $Cu_2O/Ga_2O_3$ heterojunction PDs

Fig. 3(a) shows a schematic diagram of the PD structure of $Cu_2O/Ga_2O_3$ PDs, where $Cu_2O$ particles are distributed on the top and sidewalls of $Ga_2O_3$ nanorod arrays, and FTO and Au are used as the bottom and top electrodes, respectively. Fig. 3(b)–(d) and Fig. S5 (ESI†) show the *I–V* curves of $Cu_2O/Ga_2O_3$ heterojunction PDs prepared by $Cu_2O$ electrolyte with different pH in the dark state, solar-blind UV light 254, 265 525, 550 and 660 nm illuminations. All PDs show obvious photosensitive characteristics and have photovoltaic effect under solar-blind

 

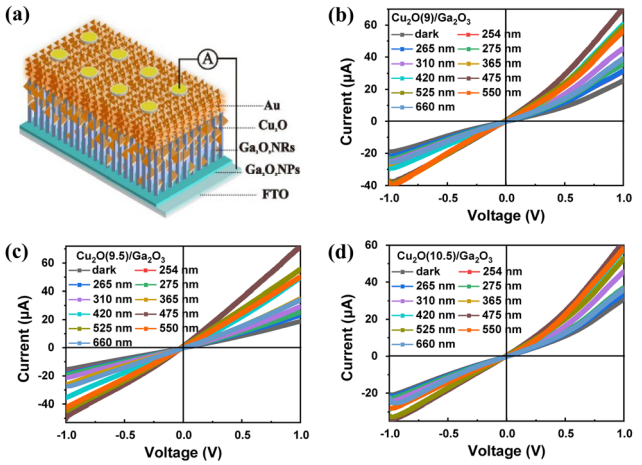


Fig. 3 (a) Schematic diagram of the PD structure of $Cu_2O/Ga_2O_3$ PDs. Dark-state and different wavelengths light illuminations *I*–*V* curves for (b) $Cu_2O(9)/Ga_2O_3$ PDs, (c) $Cu_2O(9.5)/Ga_2O_3$ PDs and (d) $Cu_2O(10.5)/Ga_2O_3$ PDs under an optical power density of 4 mW $cm^{-2}$ illumination.

UV, UV and visible illuminations, indicating that the PD can realize photodetection in the solar-blind UV-visible region under the condition of self-driving without an external electric field.

Fig. 4 shows the *I*–*t* curves of the $Cu_2O/Ga_2O_3$ heterojunction PDs under monochromatic light from solar-blind UV to visible range without external bias. All PDs can demonstrate the self-powered photoresponse in solar-blind UV-visible region with good repeatability and stability under the light switching. The

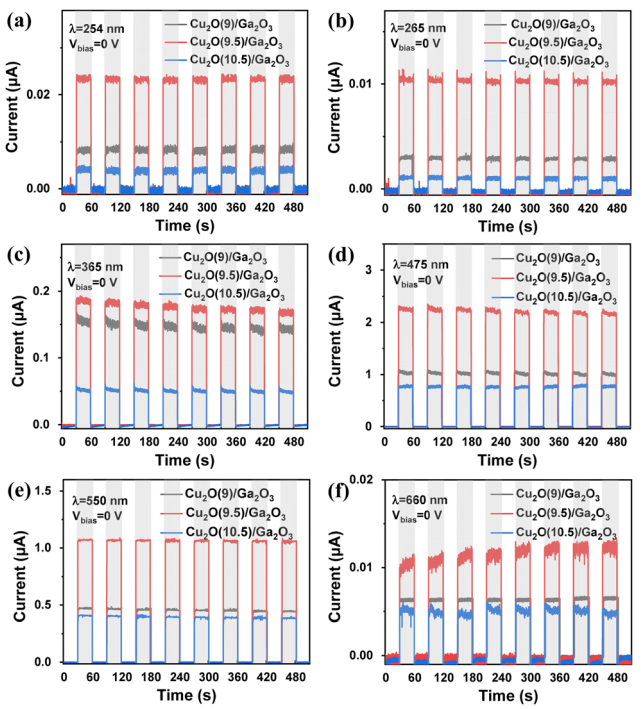


Fig. 4 *I*–*t* cycling curves at zero bias for $Cu_2O/Ga_2O_3$ heterojunction PDs with $Cu_2O$ at different pH values under (a) 254, (b) 265, (c) 365, (d) 475, (e) 550 and (f) 660 nm illuminations with $P$ = 4 mW $cm^{-2}$.

largest photocurrent is obtained under 475 nm light for all the PDs. The $Cu_2O(9.5)/Ga_2O_3$ PD exhibits an optimized photocurrent under the monochromatic light irradiation compared to other PDs. As revealed from the absorption spectra of $Cu_2O/Ga_2O_3$ heterojunctions, the photocurrent of the PD in the solar-blind UV band is mainly contributed by photogenerated carriers in $Ga_2O_3$ NRs, and that in UV and visible bands is mainly originated from the photogenerated carriers in $Cu_2O$ films. The photoresponse time is an important parameter to evaluate the performance of PDs. Fig. S7 (ESI†) shows the photoresponse time of heterojunction PDs with different pH values of $Cu_2O$ electrolyte solution under 254 and 475 nm illuminations. The photoresponse time of the PDs is in the order of millisecond. The rise time $\tau_{rise}$ under illumination is shorter than the decay time $\tau_{decay}$ of photocurrent after the light is turned off. The $\tau_{rise}$ and $\tau_{decay}$ of $Cu_2O(9.5)/Ga_2O_3$ PD are the shortest and the photoresponse speed is the fastest. Table S1 (ESI†) lists the comparison of the photoresponse time of our $Cu_2O(9.5)/Ga_2O_3$ PD and other $Ga_2O_3$ based PDs. The $Cu_2O/Ga_2O_3$ PD in this work shows a relatively fast photoresponse time.

Fig. 5(a)–(d) shows the responsivity ($R$), detectivity ($D^*$), sensitivity ($S$) and linear dynamic range (LDR) of all PDs under different illumination wavelengths from the solar-blind UV to visible range under self-powered conditions. The PDs have

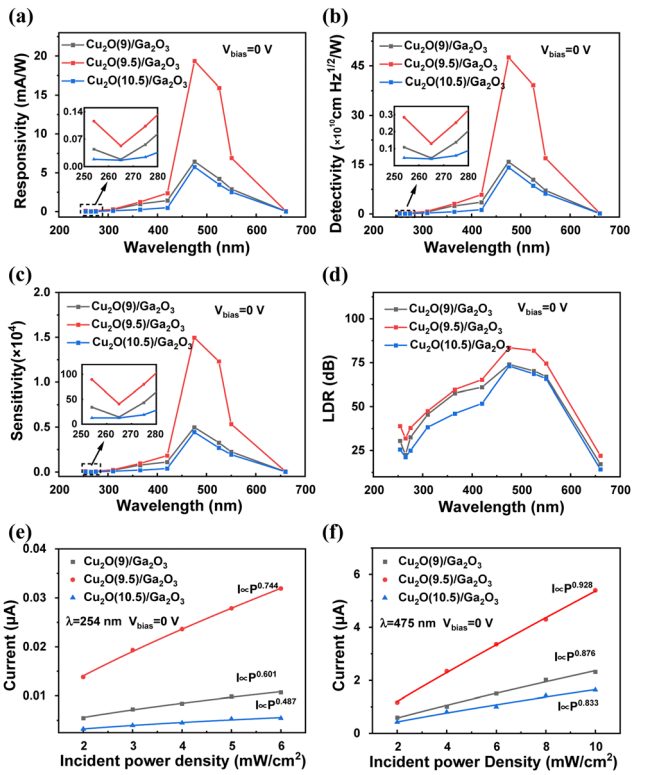


Fig. 5 Performance parameters of (a) $R$, (b) $D^*$, (c) $S$ and (d) LDR of $Cu_2O/Ga_2O_3$ heterojunction PDs with $Cu_2O$ prepared at different pH values at 0 V bias voltage under solar-blind UV, UV and visible light illuminations with 4 mW $cm^{-2}$ optical power density. Photocurrent under (e) 254 and (f) 475 nm illuminations of $Cu_2O/Ga_2O_3$ heterojunction PDs at different optical power densities.

photoresponse characteristics in the illumination range of 254–660 nm. The parameters of the PDs firstly increase and then decrease with the increase of light wavelength, reaching the optimal values at 475 nm. The LDR of $Cu_2O/Ga_2O_3$ heterojunction PDs is greater than 3 dB in both UV and visible light, which can meet the commercial standard for optical communication.

Fig. 5(e) and (f) show the curves of the relationship between photocurrent and optical power density of $Cu_2O/Ga_2O_3$ heterojunction PDs under solar-blind UV 254 nm and visible 475 nm illumination without applied voltage, respectively. The photocurrent of the heterojunction PDs increases with increasing light density, and the heterojunction produce more photogenerated carriers when illuminated by incident light of high optical power density. The nonlinear relationship between the photocurrent ($I_P$) of a PD and the optical power density ($P$) can be expressed by a power function $I_P = AP^{\theta}$. $A$ is a constant at a specific wavelength, and $\theta$ is related to the kinetic processes of photogenerated carriers including photogenerated carrier production, separation, capture, and complexation. Usually $0 < \theta < 1$, the closer the $\theta$ value is to 1, the more the photogenerated carriers contribute to the photocurrent.[40] The $Cu_2O(9.5)/Ga_2O_3$ PD derives the highest $\theta$ values, which are 0.744 and 0.928 at 254 and 475 nm, respectively. The $\theta$ values of the $Cu_2O/Ga_2O_3$ heterojunction PDs during visible light irradiation are larger than those under solar-blind UV illuminations, indicating higher photoelectric conversion efficiency for the heterojunction under the visible light illuminations.[41–49]

To further analyse the relationship between the self-powered photoresponse characteristics of the PDs and the energy band structure of the heterojunction, the information of the energy band structure based on the XPS, UPS and diffuse reflectance spectroscopy measurements are shown in Fig. 6. Considering that the Fermi level position of $Ga_2O_3$ is higher than that of $Cu_2O$, the energy band of $Ga_2O_3$ bends upwards and that of $Cu_2O$ bends downwards at the interface after the both semiconductors come into contact and reach thermal equilibrium, forming a barrier region of $Ga_2O_3$ electrons at the interface. When illuminated at 254 nm, the electrons on the valence band of $Ga_2O_3$ and $Cu_2O$ are excited to the conduction band. The excited electrons in $Ga_2O_3$ need to tunnel through the interface barrier to $Cu_2O$ conduction band with the lower energy, and finally are collected by Au electrode. The holes in $Cu_2O$ are transferred to the $Ga_2O_3$ and then *via* $Ga_2O_3$ to FTO electrode. Considering 254 nm light illumination through $Ga_2O_3$ to $Cu_2O$, few photogenerated carriers can be produced in $Cu_2O$. The photocurrent of PDs under solar-blind UV light is mainly contributed by the photogenerated carriers of $Ga_2O_3$. When irradiated at 475 nm, $Ga_2O_3$ acts as a heterojunction window, and photogenerated carriers in $Cu_2O$ contribute to the photocurrent of PDs. Due to the existence of a heterojunction interface barrier, photogenerated electrons of $Cu_2O$ are collected by the Au electrode, and photogenerated holes are transferred to the FTO electrode through $Ga_2O_3$.

Compared with the traditional optical communication system, UV light communication has the unique advantages of high flexibility, low eavesdropping, omni-directional and non-line-of-sight communication, high reliability and good confidentiality, which has wide application prospects in the communication field. With the rapid development of optical communication, there is still a risk of information interception due to the exposure of information data in free space, which poses higher requirements for information security transmission. A proof-of-concept solar-blind UV-visible encrypted communication system is designed based on $Cu_2O/Ga_2O_3$ heterojunction PDs with the solar-blind UV-visible photoresponse characteristics. The PD can be used as a receiving terminal to decode the information as a binary "1" state for a photocurrent value greater than 0.5 μA and a binary "0" state for a value less than 0.5 μA. Solar-blind UV light is used as a carrier to transmit the encrypted message A, and visible light as a carrier to transmit the key message B with the same number of binary bits. The encryption agreement is defined as follows: when the binary bit in B is "0", the information corresponding to that of A ("0" or "1") is false, and its inverse code ("1" or "0") is output. On the other hand, when the binary bit in B is "1", the information corresponding to that of A ("0" or "1") is true, and the original code ("0" or "1") is output. For example, the solar-blind UV light transmits the encrypted message A as "11011000", the visible light transmits the same number of binary bit key message B as "01110000", and the real message decoded by the encryption agreement is "01010111". The

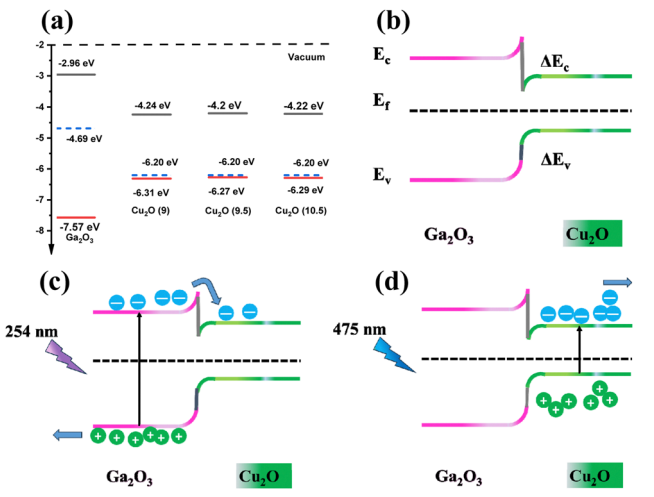


Fig. 6 Energy band structures of $Ga_2O_3$ and $Cu_2O$ prepared at different pH values (a) before and (b) contact. The schematic diagram of carrier transport of $Cu_2O/Ga_2O_3$ heterojunction under (c) 254 (d) 475 nm illuminations.

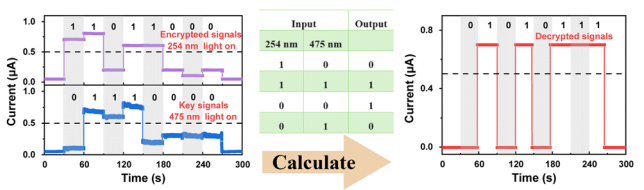


Fig. 7 Schematic diagram of the calculation process of secure optical communication.

schematic diagram of the calculation process of secure optical communication is shown in Fig. 7. Only PDs with solar-blind UV-visible band photoresponse and agreed-upon encryption algorithms can obtain real information, indicating significant potential for application in safety communication within the realm of secure and efficient data transmission.

# 3. Experimental

### 3.1 Preparation of $Ga_2O_3$ NRs

The $Ga_2O_3$ NRs were grown on the seed layer by using a hydrothermal method. Firstly, the $Ga_2O_3$ seed layers were prepared by using a sol–gel method on FTO substrates using the precursor solution obtained from 0.3086 g of gallium nitrate hydrate (Aladdin, ≥99%), 12 mL of ethylene glycol methyl ether (Aladdin, ≥99.3%), and 72 μL of ethanolamine (Aladdin, ≥99.5%) stirred in a water bath at 60 °C for 1 h. The as-grown films were annealed for 1 h at 500 °C in air. Secondly, $Ga_2O_3$ seed layers were placed in the growth solution of 0.03 M $Ga(NO_3)_3{\cdot}xH_2O$, 0.005 M $C_6H_{12}N_4$ and 30 mL DI water, and kept for 6 h at 150 °C. Finally, $Ga_2O_3$ NRs were obtained by annealing at 500 °C in air for 4 h.

### 3.2 Preparation of $Cu_2O/Ga_2O_3$

$Cu_2O$ thin films were prepared on $Ga_2O_3$ NRs by electrochemical deposition in the solution with different pH values. Firstly, 10 g $CuSO_4{\cdot}5H_2O$ (Aladdin, 85–90%) was dissolved in a certain amount of DI water and stirred for 30 min, then 22.4 mL lactic acid was added, and then an appropriate amount of DI water was added to 100 mL. The stirring was continued for 30 min, and the pH value of the solution was adjusted to 9, 9.5 and 10.5 with NaOH to obtain deposition electrolytes. $Cu_2O$ thin films were electrochemically deposited at 60 °C in a three-electrode system using $Ga_2O_3$ NRs as the working electrode, platinum plated titanium mesh as the counter electrode and Ag/AgCl as the reference electrode. The deposition current was 6 mA and the deposition time was 10 min. According to the different pH values of electrolytes, $Cu_2O/Ga_2O_3$ samples were named $Cu_2O(9)/Ga_2O_3$, $Cu_2O(9.5)/Ga_2O_3$ and $Cu_2O(10.5)/Ga_2O_3$. Finally, Au electrodes were sputtered on the heterojunction films to construct PDs.

### 3.3 Characterization and measurements

The surface morphology of the samples was characterized *via* field emission scanning electron microscopy (SEM, Hitachi S-8010). The crystal structure was studied *via* X-ray diffractometry (XRD, Rigaku D/max 2500/PC). The elemental composition and chemical state were analyzed through X-ray electron spectroscopy (XPS, Thermo ESCALAB-250), in which the photon energy of the monochromatic source (Al target) was 1846 eV. The band structure of the samples was tested by using He–I ($h\nu$ = 21.22 eV) UV photoelectron spectroscopy (UPS). The absorption and diffuse reflectance spectra of $Cu_2O$ thin films and $Ga_2O_3$ NRs were measured using a Hitachi V4100 and a Shimadzu UV-3600i Plus UV-visible spectrophotometer, respectively. Electrochemical impedance spectroscopy (EIS) data were obtained in 1 M $Na_2SO_4$ solution with an electrochemical workstation (Autolab PGSTAT 128N) using a three-electrode system with the sample as the working electrode, a platinum wire as the counter electrode, and Ag/AgCl as the reference electrode. The current–voltage ($I$–$V$) and current–time ($I$–$t$) curves in darkness and illumination were measured using a Keithley 2450 source meter and a light emitting diode (LED). The photoresponse time was obtained using an oscilloscope (Tektronix MDO3014).

# 4. Conclusions

In summary, $Cu_2O/Ga_2O_3$ heterojunction PDs with a self-powered solar-blind UV-visible photoresponse have been constructed. By adjusting the pH value of the $Cu_2O$ electrolyte, the crystallization quality and grain orientation of $Cu_2O(9.5)$ films were improved, and the interface transfer resistance of $Cu_2O(9.5)/Ga_2O_3$ heterojunction was reduced. The optimized solar-blind UV-visible photoresponse characteristics without the external bias were achieved in $Cu_2O(9.5)/Ga_2O_3$ PDs, demonstrating a responsivity of 0.12 mA $W^{-1}$, rise/decay time of 2.48/11.72 ms under 254 nm illumination, and responsivity of 19 mA $W^{-1}$, the rise/decay time of 0.96/9.12 ms under 475 nm illumination. A secure solar-blind UV-visible optical communication system with two independent optical channels is proposed by using the photoresponse characteristics of solar-blind UV-visible band PDs, in which solar-blind UV is used as the information carrier and visible light as the key. Information can be transmitted through an encryption algorithm *via* secure and reliable communication. This method has a good application prospects in the field of secure communication.

# Author contributions

Xiaodan Wang: conceptualization, data curation, formal analysis, writing – original draft. Jianping Xu: conceptualization, formal analysis, resources, funding acquisition. Shaobo Shi: formal analysis. Lina Kong: formal analysis. Xiangwei He: formal analysis. Jiahang He: formal analysis. Xiaosong Zhang: formal analysis. Lan Li: formal analysis, resources, project administration, supervision.

# Conflicts of interest

The authors declare that they have no known competing financial interests or personal relationships that could have appeared to influence the work reported in this paper.

# Acknowledgements

This work was supported by the National Natural Science Foundation of China (grant numbers 52271187, 62375205, 51971158 and 51871167); the Natural Science Foundation of Tianjin (grant number 18JCYBJC86200); and the Scientific Developing Foundation of Tianjin Education Commission (grant number 2018ZD09).

## References


1 M. Dai, H. Chen, R. Feng, W. Feng, Y. Hu, H. Yang, G. Liu, X. Chen, J. Zhang, C.-Y. Xu and P. Hu, A Dual-Band Multilayer InSe Self-Powered Photodetector with High Performance Induced by Surface Plasmon Resonance and Asymmetric Schottky Junction, *ACS Nano*, 2018, **12**, 8739–8747.

2 P. Wang, S. Liu, W. Luo, H. Fang, F. Gong, N. Guo, Z. G. Chen, J. Zou, Y. Huang, X. Zhou, J. Wang, X. Chen, W. Lu, F. Xiu and W. Hu, Arrayed van der Waals Broadband Detectors for Dual-Band Detection, *Adv. Mater.*, 2017, **29**, 1604439.

3 Y. Gao, C. Zhao, K. Pu, M. He, W. Cai, M.-C. Tang, F. Kang, H.-L. Yip and G. Wei, Low-voltage-modulated Perovskite/organic Dual-band Photodetectors for Visible and Near-infrared Imaging, *Sci. Bull.*, 2022, **67**, 1982–1990.

4 S. Chen, C. Teng, M. Zhang, Y. Li, D. Xie and G. Shi, A Flexible UV-Vis-NIR Photodetector based on a Perovskite/Conjugated-Polymer Composite, *Adv. Mater.*, 2016, **28**, 5969–5974.

5 T. He, C. Li, X. Zhang, Y. Ma, X. Cao, X. Shi, C. Sun, J. Li, L. Song, C. Zeng, K. Zhang, X. Zhang and B. Zhang, Metalorganic Chemical Vapor Deposition Heteroepitaxial β-$Ga_2O_3$ and Black Phosphorus Pn Heterojunction for Solar-Blind Ultraviolet and Infrared Dual-Band Photodetector, *Phys. Status Solidi A*, 2019, **217**, 1900861.

6 B. Huang, J. Liu, Z. Han, Y. Gu, D. Yu, X. Xu and Y. Zou, High-Performance Perovskite Dual-Band Photodetectors for Potential Applications in Visible Light Communication, *ACS Appl. Mater. Interfaces*, 2020, **12**, 48765–48772.

7 C. h Xu, S. H. Luo, Y. Wang, X. F. Shi, C. Fu, J. Wang, C. Y. Wu and L. B. Luo, Bias-Selectable Si Nanowires/PbS Nanocrystalline Film n–n Heterojunction for NIR/SWIR Dual-Band Photodetection, *Adv. Funct. Mater.*, 2023, **33**, 2214996.

8 F. Cao, Z. Q. Li, X. Y. Liu, Z. F. Shi and X. S. Fang, Air Induced Formation of CsBiBr/CsBiBr Bulk Heterojunction and Its Dual-band Photodetection Abilities for Light Communication, *Adv. Funct. Mater.*, 2022, **32**, 2206151.

9 M.-M. Fan, K.-L. Xu, X.-Y. Li, G.-H. He and L. Cao, Self-powered Solar-blind UV/visible Dual-band Photodetection based on a Solid-state PEDOT:PSS/α-$Ga_2O_3$ Nanorod Array/FTO Photodetector, *J. Mater. Chem. C*, 2021, **9**, 16459–16467.

10 T. T. Yan, Z. Q. Li, L. Su, L. M. Wu and X. S. Fang, Bidirectional and Dual-Mode Organic Photodetector Enables Secure Ultraviolet Communication, *Adv. Funct. Mater.*, 2023, **33**, 2302746.

11 S. Li, D. Guo, P. Li, X. Wang, Y. Wang, Z. Yan, Z. Liu, Y. Zhi, Y. Huang, Z. Wu and W. Tang, Superhigh Signal-to-Noise Ratio, Self-Powered Solar-blind Photodetector Based on n-Ga2O3/p-CuSCN Core–Shell Microwire Heterojunction, *ACS Appl. Mater. Interfaces*, 2019, **11**, 35105–35114.

12 M. S. Long, P. Wang, H. H. Fang and W. D. Hu, Progress, Challenges, and Opportunities for 2D Material Based Photodetectors, *Adv. Funct. Mater.*, 2019, **29**, 1803807.

13 X. Yu, Y. Li, X. Hu, D. Zhang, Y. Tao, Z. Liu, Y. He, M. A. Haque, Z. Liu, T. Wu and Q. J. Wang, Narrow Bandgap Oxide Nanoparticles Coupled with Graphene for High Performance Mid-infrared Photodetection, *Nat. Commun.*, 2018, **9**, 4299.

14 W. X. Ouyang, F. Teng, J. H. He and X. S. Fang, Enhancing the Photoelectric Performance of Photodetectors Based on Metal Oxide Semiconductors by Charge-Carrier Engineering, *Adv. Funct. Mater.*, 2019, **29**, 1807672.

15 M. Anaya, J. P. Correa-Baena, G. Lozano, M. Saliba, P. Anguita, B. Roose, A. Abate, U. Steiner, M. Grätzel, M. E. Calvo, A. Hagfeldt and H. Míguez, Optical Analysis of $CH_3NH_3Sn_xPb_{1-x}I_3$ Absorbers: A Roadmap for Perovskite-on-perovskite Tandem Solar cells, *J. Mater. Chem. A*, 2016, **4**, 11214–11221.

16 Z. Yang, A. Rajagopal, C. C. Chueh, S. B. Jo, B. Liu, T. Zhao and A. K. Jen, Stable Low-Bandgap Pb-Sn Binary Perovskites for Tandem Solar Cells, *Adv. Mater.*, 2016, **28**, 8990–8997.

17 Y. Zhang, D. S. Jiang, J. B. Xia, L. Q. Cui, C. Y. Song, Z. Q. Zhou and W. K. Ge, A Voltage-controlled Tunable Two-color Infrared Photodetector using GaAs/AlAs/GaAlAs and GaAs/GaAlAs Stacked Multiquantum Wells, *Appl. Phys. Lett.*, 1996, **68**, 2114–2116.

18 L. Wang, J. Jie, Z. Shao, Q. Zhang, X. Zhang, Y. Wang, Z. Sun and S. T. Lee, $MoS_2$/Si Heterojunction with Vertically Standing Layered Structure for Ultrafast, High-Detectivity, Self-Driven Visible–Near Infrared Photodetectors, *Adv. Funct. Mater.*, 2015, **25**, 2910–2919.

19 D. Y. Guo, H. Z. Shi, Y. P. Qian, M. Lv, P. G. Li, Y. L. Su, Q. Liu, K. Chen, S. L. Wang, C. Cui, C. R. Li and W. H. Tang, Fabrication of β-Ga2O3/ZnO Heterojunction for Solar-blind Deep Ultraviolet Photodetection, *Semicond. Sci. Technol.*, 2017, **32**, 03LT01.

20 A. Hierro, G. Tabares, M. Lopez-Ponce, J. M. J. M. Ulloa, A. Kurtz, E. Muñoz, V. Marín-Borrás, V. Muñoz-Sanjosé and J.-M. Chauveau, *ZnMgO-based UV Photodiodes: a Comparison of Films Grown by Spray Pyrolysis and MBE*, San Francisco, CA, February, 2016.

21 T. Onuma, S. Saito, K. Sasaki, T. Masui, T. Yamaguchi, T. Honda and M. Higashiwaki, Valence Band Ordering in β-$Ga_2O_3$ Studied by Polarized Transmittance and Reflectance Spectroscopy, *Jpn. J. Appl. Phys.*, 2015, **54**, 112601.

22 Q.-M. Fu, D.-C. He, Z.-C. Yao, J.-L. Peng, H.-Y. Zhao, H. Tao, Z. Chen, Y.-F. Tu, Y. Tian, D. Zhou, G. Zheng and Z.-B. Ma, Self-powered Ultraviolet Photodetector based on ZnO Nanorod Arrays Decorated with Sea Anemone-like CuO Nanostructures, *Mater. Lett.*, 2018, **222**, 74–77.

23 D. Chen, L. Wei, L. Meng, D. Wang, Y. Chen, Y. Tian, S. Yan, L. Mei and J. Jiao, High-Performance Self-Powered UV Detector based on $SnO_2$-$TiO_2$ Nanomace Arrays, *Nanoscale Res. Lett.*, 2018, **13**, 92.

24 Y. Zhang, J. Xu, S. Shi, Y. Gao, C. Wang, X. Zhang, S. Yin and L. Li, Development of Solution-Processed ZnO Nanorod Arrays Based Photodetectors and the Improvement of UV Photoresponse via AZO Seed Layers, *ACS Appl. Mater. Interfaces*, 2016, **8**, 22647–22657.


 

25 Z. Xi, Z. Liu, L. Yang, K. Tang, L. Li, G. Shen, M. Zhang, S. Li, Y. Guo and W. Tang, Comprehensive Study on Ultra-Wide Band Gap $La_2O_3$/ε-$Ga_2O_3$ p–n Heterojunction Self-Powered Deep-UV Photodiodes for Flame Sensing, *ACS Appl. Mater. Interfaces*, 2023, **15**, 40744–40752.

26 W. Gong, J. Yan, F. Gao, S. Ding, G. He and L. Li, High-Performance UV–Vis Broad-Spectra Photodetector Based on a β-$Ga_2O_3$/Au/$MAPbBr_3$ Sandwich Structure, *ACS Appl. Mater. Interfaces*, 2022, **14**, 47853–47862.

27 S. K. Baek, Y. H. Kwon, J. H. Shin, H. S. Lee and H. K. Cho, Low-Temperature Processable High-Performance Electrochemically Deposited p-Type Cuprous Oxides Achieved by Incorporating a Small Amount of Antimony, *Adv. Funct. Mater.*, 2015, **25**, 5214–5221.

28 L. L. Wu, L. K. Tsui, N. Swami and G. Zangari, Photoelectrochemical Stability of Electrodeposited CuO Films, *J. Phys. Chem. C*, 2010, **114**, 11551–11556.

29 Y. Zhou and J. A. Switzer, Electrochemical Deposition and Microstructure of Copper(I) Oxide Films, *Scr. Mater.*, 1998, **38**, 1731–1738.

30 T. Kobayashi, T. Gake, Y. Kumagai, F. Oba and Y.-I. Matsushita, Energetics and Electronic Structure of Native Point Defects in α-$Ga_2O_3$, *Appl. Phys. Express*, 2019, **12**, 091001.

31 P. Grez, F. Herrera, G. Riveros, A. Ramírez, R. Henríquez, E. Dalchiele and R. Schrebler, Morphological, Structural, and Photoelectrochemical Characterization of n-type CuO Thin Films Obtained by Electrodeposition, *Phys. Status Solidi A*, 2012, **209**, 2470–2475.

32 Y.-C. Chen, Y.-J. Chen, P.-H. Dong and Y.-K. Hsu, Benchmarked Photoelectrochemical Water Splitting by Nickel-Doped n-Type Cuprous Oxide, *ACS Appl. Energy Mater.*, 2020, **3**, 1373–1380.

33 Y. Wang, N. Li, P. Duan, X. Sun, B. Chu and Q. He, Properties and Photocatalytic Activity of β-$Ga_2O_3$ Nanorods under Simulated Solar Irradiation, *J. Nanomater.*, 2015, **2015**, 191793.

34 D. Y. Guo, Z. P. Wu, Y. H. An, P. G. Li, P. C. Wang, X. L. Chu, X. C. Guo, Y. S. Zhi, M. Lei, L. H. Li and W. H. Tang, Unipolar Resistive Switching Behavior of Amorphous Gallium Oxide Thin Films for Nonvolatile Memory Applications, *Appl. Phys. Lett.*, 2015, **106**, 042105.

35 D. Y. Guo, Z. P. Wu, Y. H. An, X. C. Guo, X. L. Chu, C. L. Sun, L. H. Li, P. G. Li and W. H. Tang, Oxygen Vacancy Tuned Ohmic-Schottky Conversion for Enhanced Performance in β-$Ga_2O_3$ Solar-blind Ultraviolet Photodetectors, *Appl. Phys. Lett.*, 2014, **105**, 023507.

36 Y. Liu, J. Zhu, L. Cai, Z. Yao, C. Duan, Z. Zhao, C. Zhao and W. Mai, Solution-Processed High-Quality $Cu_2O$ Thin Films as Hole Transport Layers for Pushing the Conversion Efficiency Limit of $Cu_2O$/Si Heterojunction Solar Cells, *Sol. RRL*, 2019, **4**, 1900339.

37 D.-W. Jeon, H. Son, J. Hwang, A. Y. Polyakov, N. B. Smirnov, I. V. Shchemerov, A. V. Chernykh, A. I. Kochkova, S. J. Pearton and I.-H. Lee, Electrical Properties, Structural Properties, and Deep Trap Spectra of Thin α-$Ga_2O_3$ Films Grown by Halide Vapor Phase Epitaxy on Basal Plane Sapphire Substrates, *APL Mater.*, 2018, **6**, 121110.

38 T. Zhang, J. Lin, X. Zhang, Y. Huang, X. Xu, Y. Xue, J. Zou and C. Tang, Single-crystalline Spherical β-$Ga_2O_3$ Particles: Synthesis, N-doping and Photoluminescence Properties, *J. Lumin.*, 2013, **140**, 30–37.

39 X. Ren, P. Gao, X. Kong, R. Jiang, P. Yang, Y. Chen, Q. Chi and B. Li, NiO/Ni/$TiO_2$ Nanocables with Schottky/p-n Heterojunctions and the Improved Photocatalytic Performance in Water Splitting under Visible Light, *J. Colloid Interface Sci.*, 2018, **530**, 1–8.

40 Z. Long, X. Xu, W. Yang, M. Hu, D. V. Shtansky, D. Golberg and X. Fang, Cross-Bar $SnO_2$-NiO Nanofiber-Array-Based Transparent Photodetectors with High Detectivity, *Adv. Electron. Mater.*, 2019, **6**, 1901048.

41 P. Li, H. Shi, K. Chen, D. Guo, W. Cui, Y. Zhi, S. Wang, Z. Wu, Z. Chen and W. Tang, Construction of GaN/$Ga_2O_3$ p-n Junction for an Extremely High Responsivity Self-powered UV Photodetector, *J. Mater. Chem. C*, 2017, **5**, 10562–10570.

42 Y. Wang, C. Wu, D. Guo, P. Li, S. Wang, A. Liu, C. Li, F. Wu and W. Tang, All-Oxide NiO/$Ga_2O_3$ p–n Junction for Self-Powered UV Photodetector, *ACS Appl. Electron. Mater.*, 2020, **2**, 2032–2038.

43 Z. Yan, S. Li, Z. Liu, Y. Zhi, J. Dai, X. Sun, S. Sun, D. Guo, X. Wang, P. Li, Z. Wu, L. Li and W. Tang, High Sensitivity and Fast Response Self-powered Solar-blind Ultraviolet Photodetector with a β-$Ga_2O_3$/spiro-MeOTAD p–n Heterojunction, *J. Mater. Chem. C*, 2020, **8**, 4502–4509.

44 S. Li, Z. Yan, Z. Liu, J. Chen, Y. Zhi, D. Guo, P. Li, Z. Wu and W. Tang, A Self-powered Solar-blind Photodetector with Large Voc Eenhancing Performance Based on the PEDOT:PSS/$Ga_2O_3$ Organic–inorganic Hybrid Heterojunction, *J. Mater. Chem. C*, 2020, **8**, 1292–1300.

45 C. Wu, F. Wu, L. Deng, S. Li, S. Wang, L. Cheng, A. Liu, J. Wang, W. Tang and D. Guo, Solution-processed Y-doped $SnSrO_3$ Electron Transport Layer for $Ga_2O_3$ Based Heterojunction Solar-blind Photodetector with High Sensitivity, *Vacuum*, 2022, **201**, 111064.

46 K. Arora, N. Goel, M. Kumar and M. Kumar, Ultrahigh Performance of Self-Powered β-$Ga_2O_3$ Thin Film Solar-Blind Photodetector Grown on Cost-Effective Si Substrate Using High-Temperature Seed Layer, *ACS Photonics*, 2018, **5**, 2391–2401.

47 L. Wu, X. Jiao, D. Wang, W. Guo, L. Li, F. Li and W. Tang, A Self-powered Deep-ultraviolet Photodetector Based on an Epitaxial $Ga_2O_3$/Ga:ZnO Heterojunction, *J. Mater. Chem. C*, 2017, **5**, 8688–8693.

48 J. Yu, M. Yu, Z. Wang, L. Yuan, Y. Huang, L. Zhang, Y. Zhang and R. Jia, Improved Photoresponse Performance of Self-Powered β-$Ga_2O_3$/NiO Heterojunction UV Photodetector by Surface Plasmonic Effect of Pt Nanoparticles, *IEEE Trans. Electron. Devices*, 2020, **67**, 3199–3204.

49 D. Guo, H. Liu, P. Li, Z. Wu, S. Wang, C. Cui, C. Li and W. Tang, Zero-Power-Consumption Solar-Blind Photodetector Based on β-$Ga_2O_3$/NSTO Heterojunction, *ACS Appl. Mater. Interfaces*, 2017, **9**, 1619–1628.